

NUMERICAL INVESTIGATION OF LAMINAR SHOCK/BOUNDARY LAYER INTERACTION

Gustavo Bono, bonogustavo@gmail.com

Federal University of Rio Grande do Sul,
Graduate Program in Mechanical Engineering,
Av. Sarmento Leite 425, 90050-170 Porto Alegre, RS,
Brazil

Armando M. Awruch, amawruch@ufrgs.br

Federal University of Rio Grande do Sul,
Applied and Computacional Mechanical Center,
Av. Osvaldo Aranha 99, 90035-190 Porto Alegre, RS,
Brazil

Abstract. *The main objective of this paper is to study hypersonic viscous flows dominated by shock-wave / laminar boundary-layer interaction over a compression corner. The shock-wave / boundary-layer interaction is studied using numerical solutions of the Navier-Stokes equations for unsteady flows using a Mach number equal to 10.30. The flows are simulated using the Finite Element Method with two explicit Taylor-Galerkin schemes (a one-step iterative scheme and a two-step non iterative scheme) with linear tetrahedral and tri-linear hexahedral elements. Results include surface pressure, skin friction and velocity/pressure/density profiles in several stations.*

Keywords: *hypersonic flow, laminar boundary layer / shock wave interaction, finite element method*

1. INTRODUCTION

The problem of shock wave / boundary layer interactions (SWBLI) in supersonic and hypersonic flows has been studied for decades (Dolling, 2001) due to its direct application in various configurations such as aircraft/spacecraft (control surfaces and wing-fuselage junction), missiles and projectiles, among others. In these configurations the SWBLI has a strong influence in the following items: the levels of heating, the size of the recirculation regions, the loss of efficiency of control surfaces and the oscillation of transient pressure loads. The geometry formed by the flat plate and the ramp is a typical example in the study of the SWBLI. Although the geometry is simple, the physical phenomena in this problem are very complex; they are the boundary layer separation induced by the shock wave / boundary layer interaction and the strong gradients generated in the recompression region. The main parameters affecting the SWBLI are: the Mach number, the Reynolds number, the surface temperature, the boundary layer (laminar or turbulent), the deflection angle of the ramp and the chemical state of the gas.

Due to great interest in hypersonic problems, the NATO Research Technology Organization - Advanced Vehicle Technology - Panel Working Group 10 (RTO-TR-AVT-007-V3), proposed some examples for validation of Computational Fluid Dynamics capability for specific flow phenomena relevant to hypersonic flight, which allows a detailed analysis of the influence of different schemes and meshes. The geometry is slightly modified with respect to that employed by Chantz *et al.* (1998). The experiments were conducted for Mach numbers ranging from 10.16 and 12.49 over a range of Reynolds numbers low enough to ensure the flows remained laminar over the model. The local temperature does not exceed high values where chemical and non-thermal equilibrium effects are initiated.

In the present work, Navier-Stokes simulations are applied for cold hypersonic gas flow past a compression corner. An in-house developed Navier-Stokes code with structured and unstructured meshes is employed for these computations. The aim of the present work is to study the performance of two explicit Taylor-Galerkin schemes and two types of elements at hypersonic flow. One case is studied and results are compared with experimental and computational results available in the literature.

2. THE GOVERNING EQUATIONS

Let $\Omega \subset R^{n_{sd}}$ and $(0,T)$ be the spatial and temporal domains, respectively, where $n_{sd} = 3$ is the number of space dimensions, and let Γ denote the boundary of Ω . The spatial and temporal coordinates are denoted by \mathbf{x} and t . We consider the conservative form of the Navier-Stokes equations governing unsteady compressible flows with no source terms, written here in their dimensionless form

$$\frac{\partial \mathbf{U}}{\partial t} + \frac{\partial \mathbf{F}_i}{\partial x_i} + \frac{\partial \mathbf{G}_i}{\partial x_i} = 0 \quad (1)$$

where \mathbf{U} is the unknown vector of the conservation variables, \mathbf{F}_i and \mathbf{G}_i are, respectively, the advective and diffusive flux vectors given by

$$\mathbf{U} = \begin{Bmatrix} \rho \\ \rho v_i \\ \rho e \end{Bmatrix}, \quad \mathbf{F}_i = \begin{Bmatrix} \rho v_j \\ \rho v_i v_j + p \delta_{ij} \\ v_j (\rho e + p) \end{Bmatrix}, \quad \mathbf{G}_i = \begin{Bmatrix} 0 \\ -\tau_{ij} \\ -\tau_{ji} v_i - q_j \end{Bmatrix} \quad (2)$$

with $i, j = 1, 2, 3$. Here v_i is the velocity component in the direction of the coordinate x_i , ρ is the specific mass, p is the thermodynamic pressure, τ_{ij} are the components of the viscous stress tensor, q_j is the heat flux vector, e is the total specific energy and δ_{ij} is the Kronecker delta function.

For a calorically perfect gas, the equation of state and internal energy i are given by the following equations

$$p = (\gamma - 1) \rho i, \quad i = c_v T = e - \frac{1}{2} v_i v_i \quad (3)$$

where p is the pressure, T is the temperature and $\gamma = c_p / c_v$ with c_p and c_v being the specific heat coefficients at constant pressure and constant volume, respectively. The dynamic viscosity and coefficient of thermal conductivity depend a temperature and therefore are modeled using Sutherland's law. Initial and boundary conditions must be added to Eq. (1) in order to define uniquely the problem.

3. A TAYLOR-GALERKIN FORMULATION

The numerical scheme is obtained expanding in Taylor series the governing equation and applying after the space discretization process, using the Finite Element Method (FEM) in the context of the classical Bubnov-Galerkin scheme. Two schemes for explicit time integration (one-step and two-step methods) are investigated for solving the compressible viscous flow problems. The formulation exclusively employs tetrahedral and hexahedral finite elements which provide second-order spatial accuracy.

3.1. Time discretization: One-step scheme

The one-step scheme is similar to that presented by Donea (1984). Expanding the conservation variables \mathbf{U} at $t = t^{n+1}$ in Taylor series including the first and second derivatives, and substituing Eq. (1) and its second derivative, and neglecting high-order terms, we obtain

$$\begin{aligned} \Delta \mathbf{U}_{I+1}^{n+1} = & \Delta t \left[-\frac{\partial \mathbf{F}_i^n}{\partial x_i} - \frac{\partial \mathbf{G}_i^n}{\partial x_i} + \frac{\Delta t}{2} \frac{\partial}{\partial x_k} \left(\mathbf{A}_k^n \frac{\partial \mathbf{F}_i^n}{\partial x_i} \right) \right] + \\ & + \frac{\Delta t}{2} \left[-\frac{\partial \Delta \mathbf{F}_{iI}^{n+1}}{\partial x_i} - \frac{\partial \Delta \mathbf{G}_{iI}^{n+1}}{\partial x_i} + \frac{\Delta t}{2} \frac{\partial}{\partial x_k} \left(\mathbf{A}_k^n \frac{\partial \Delta \mathbf{F}_{iI}^{n+1}}{\partial x_i} \right) \right] \end{aligned} \quad (4)$$

with $\Delta \mathbf{U}^{n+1} = \mathbf{U}^{n+1} - \mathbf{U}^n$, the time step $\Delta t = t^{n+1} - t^n$, n and $n+1$ indicates t and $t+\Delta t$, respectively. I is an iteration counter, $\Delta \mathbf{F}_i^{n+1} = \mathbf{F}_i^{n+1} - \mathbf{F}_i^n$, $\Delta \mathbf{G}_i^{n+1} = \mathbf{G}_i^{n+1} - \mathbf{G}_i^n$ and \mathbf{A}_i is the convection Jacobian defined as $\mathbf{A}_i = \partial \mathbf{F}_i / \partial \mathbf{U}$. In expression (4), the variables at time level $n+1$ are involved in the left and right sides of the equation; therefore it is necessary to use an iterative scheme.

3.2. Time discretization: Two-step scheme

The two-step scheme is similar to that presented by Kawahara and Hirano (1983). In the first step, corresponding to the time interval $[t^n, t^{n+1/2}]$, the unknown vector \mathbf{U} at $t = t^{n+1/2}$ is expanded in Taylor series. Substituing equation (1) and its second derivative, and neglecting high-order terms, gives

$$\Delta \mathbf{U}^{n+1/2} = \frac{\Delta t}{2} \left[-\frac{\partial \mathbf{F}_i^n}{\partial x_i} - \frac{\partial \mathbf{G}_i^n}{\partial x_i} + \frac{\Delta t}{4} \frac{\partial}{\partial x_i} \left(\mathbf{A}_i^n \frac{\partial \mathbf{F}_j^n}{\partial x_j} \right) \right] \quad (5)$$

with $\Delta \mathbf{U}^{n+1/2} = \mathbf{U}^{n+1/2} - \mathbf{U}^n$. In the second step, \mathbf{U} at time t^{n+1} is determined by expanding equation (1) in Taylor series. Substituting equation (1) and its second derivative, and neglecting high-order terms, the following expression is obtained

$$\Delta \mathbf{U}^{n+1} = \Delta t \left[-\frac{\partial \mathbf{F}_i}{\partial x_i} - \frac{\partial \mathbf{G}_i}{\partial x_i} + \frac{\Delta t}{2} \frac{\partial}{\partial x_i} \left(\mathbf{A}_i \frac{\partial \mathbf{F}_j}{\partial x_j} \right) \right]^{n+1/2} \quad (6)$$

where $\Delta \mathbf{U}^{n+1} = \mathbf{U}^{n+1} - \mathbf{U}^n$ and the convection Jacobian \mathbf{A}_i is defined as $\mathbf{A}_i = \partial \mathbf{F}_i / \partial \mathbf{U}$.

3.3. Spatial discretization

Applying the classical Bubnov-Galerkin weighted residual method in the context of the FEM to Eq. (4), for the one-step scheme, and Eqs. (5) and (6), for the two-step scheme, spatial discretization are obtained for both cases. Details of the explicit matrix form of Eqs. (4), (5) and (6) can be found in Bono (2008). The computational domain was divided into a finite number of tri-linear hexahedral elements (structured mesh) or linear tetrahedral elements (unstructured mesh). The consistent mass matrix is substituted by the lumped mass matrix and then these equations are solved with an explicit scheme.

The explicit character of the algorithm implies that it will be subjected to the Courant-Friedrichs-Lewy stability criterion. At supersonic speeds, an additional numerical damping is necessary to capture shocks and to smooth local oscillations in the vicinity of shocks. An artificial viscosity model, as proposed by Argyris *et al.* (1990), due to its simplicity and efficiency in terms of CPU time, is adopted here.

4. ADAPTIVE UNSTRUCTURED MESH REFINEMENT

The unstructured mesh-based CFD methodology has undergone considerable development in the last decade in term of both mesh generation and solution algorithm development. The concentration of the node in the mesh is very important to obtain good quality solutions. The nodes need to be concentrated in regions where some variable gradients are high with respect to a specific criterium.

Local physical phenomena in the flow are detected with error indicators or errors estimators. In this work, these error indicators take into account regions with low velocities, changes in velocity directions, velocity gradients, pressure gradients and internal energy gradients. The criterion for mesh adaptation is based in the normal distribution of the error indicators and their mean values and standard deviation. The adaptive process was performed using the *h*-refinement method. Details of the error indicators, mesh adaptation and the refinement process can be found in Popiolek and Awruch (2006).

5. NUMERICAL RESULTS

In this section one test case is presented in order to evaluate the accuracy, the capability and the performance of the two explicit Taylor-Galerkin schemes in the context of structured/unstructured meshes applied to the solution of hypersonic flows. These programs do not take into account high temperature effects, such as, vibrational excitation and chemical reaction. Although in the present work only two-dimensional (2-D) examples are presented, they were simulated with a three-dimensional solver taking one layer of elements in the *z*-direction, which is perpendicular to the flow direction. The boundary conditions are chosen so that a 2-D flow field is simulated. Fluid properties are considered constant, with $\gamma = 1.4$ and Prandtl Number $Pr = 0.72$.

5.1. Supersonic flow past a compression corner

In this example the case 14 studied by Holden *et al.* (2006) is considered. This test case has been studied extensively using experimental and computational techniques. The fluid properties are given by a Mach number equal to 10.30 and a Reynolds number equal to 24624.6 (with relation to the values of the free stream conditions and the length of the flat plate). With this example it is intended to validate the various schemes implemented and the method of adaptive refinement in hypersonic flow, as well as contribute to understanding the physical characteristics of the problem of shock wave / laminar boundary layer interaction.

The numerical schemes employed for the solution of the Navier-Stokes equations are the one-step and two-step schemes with hexahedral (H) and tetrahedral (T) elements. In order to capture de boundary layers effects the elements are concentrated near the solid contours. The mesh with tetrahedral elements is obtained by subdividing each hexahedral element into five tetrahedral elements. The identification for each example, the number of nodes (*nno*), the

number of elements ($nele$), the number of nodes on the wall ($nnoCS$), the length (Δl) of the recirculation, the maximum pressure coefficient ($C_{p_{max}}$), the minimum time step (Δt) and the artificial damping coefficient (CAF) are shown in Tab. 1.

Table 1. Numerical and physical parameters for the SWBLI simulation.

elem. / scheme	mesh	nno	$nele$	$nnoCS$	Δl	$C_{p_{max}}$	Δt	CAF
hexahedral / 1-step	M1H	31232	15300	482	0.551	0.967	$4 \cdot 10^{-5}$	0.7
	M2H	48422	23800	642	0.677	1.051	$4 \cdot 10^{-5}$	0.7
	M3H	68202	33600	782	0.706	1.058	$3 \cdot 10^{-5}$	0.7
	M3aH	68202	33600	782	0.743	1.123	$3 \cdot 10^{-5}$	0.4
hexahedral / 2-step	M2Hp2	48422	23800	642	0.741	1.055	$4 \cdot 10^{-5}$	0.7
	M2aHp2	48422	23800	642	0.764	1.128	$4 \cdot 10^{-5}$	0.4
tetrahedral / 1-step	M2T	26112	63750	482	0.349	0.834	$3 \cdot 10^{-5}$	0.7
	M2TR1	66860	220131	1443	0.509	0.875	$1 \cdot 10^{-5}$	0.7
	M2TR2	246882	1067740	4805	0.542	0.998	$6 \cdot 10^{-6}$	0.7
tetrahedral / 2-step	M2Tp2	26112	63750	482	0.269	0.786	$3 \cdot 10^{-5}$	0.7
	M2Tp2R1	66860	220131	1443	0.480	0.845	$1 \cdot 10^{-5}$	0.7
	M2Tp2R2	246882	1067740	4805	0.554	0.953	$6 \cdot 10^{-6}$	0.7

The meshes with tetrahedral elements are adapted with the following errors indicators: low velocity components, change in the velocity components, velocity gradients, pressure gradients and internal energy gradients. The first and second refinements are identified as R1 and R2, respectively.

The computed pressure coefficient and skin friction coefficient for the meshes M1H, M2H, M3H and M3aH are shown in Fig. 1. In the last mesh the CAF was reduced from 0.70 to 0.40. The pressure coefficient is very close to the experimental results obtained by Holden *et al.* (2006) near the recompression region. However, in the recirculation region, in the peak pressure and in the plateau pressure, the numerical computation overestimate the pressure coefficient. The skin friction coefficient increases rapidly downstream of the attachment. The initial mesh M1H gives the best results compared with the experimental results in the recirculation region, but disagreement occurs with the successive refinements of the mesh. The meshes M2H and M3H show a recirculation region and peak pressures greater than those presented by Holden *et al.* (2006) and mesh M1H; these results are representative of a problem with an higher Reynolds number.

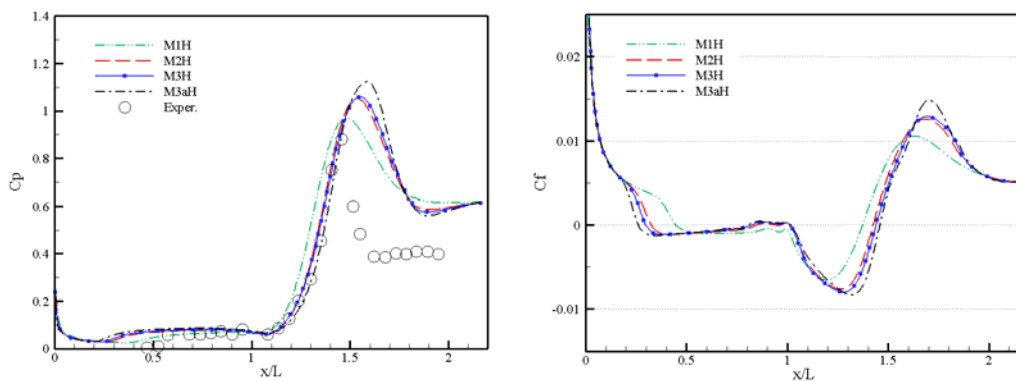


Figure 1. Pressure coefficient and skin friction coefficient on the meshes M1H, M2H, M3H and M3aH, compared with result obtained experimentally by Holden *et al.* (2006)

The differences between the experimental and numerical results can not be attributed to the mesh refinement, because the small difference between the pressure coefficient on the M2H and M3H meshes indicate that the solutions on those meshes may be regarded as nearly mesh independent. The artificial damping coefficient was reduced from 0.7 to 0.4 in the mesh M3H with the aim of study its influence. Reduction of CAF (mesh M3aH) increases slightly the peak pressure and recirculation region compared with the previous results (see Fig. 1).

The pressure coefficient and skin friction coefficient for the mesh with hexahedral elements using the two-step scheme (M2Hp2) are shown in Fig. 2. The tests with the one-step and two-step schemes with hexahedral mesh look similar. For the same artificial damping coefficient ($CAF = 0.7$), the two-step scheme (M2Hp2) is more diffusive than the one-step scheme (M2H). Reducing the coefficient CAF to 0.4, no improvements are obtained in the results (see M2aHp2).

The discrepancies obtained with the hexahedral meshes, possibly have origin in the discretization used, since the refinement and the reduction of the CAF do not improve computational results. With an higher concentration of elements at the beginning of the plate and at the intersection flat-plate/ramp, probably the separation of the boundary layer would be best captured.

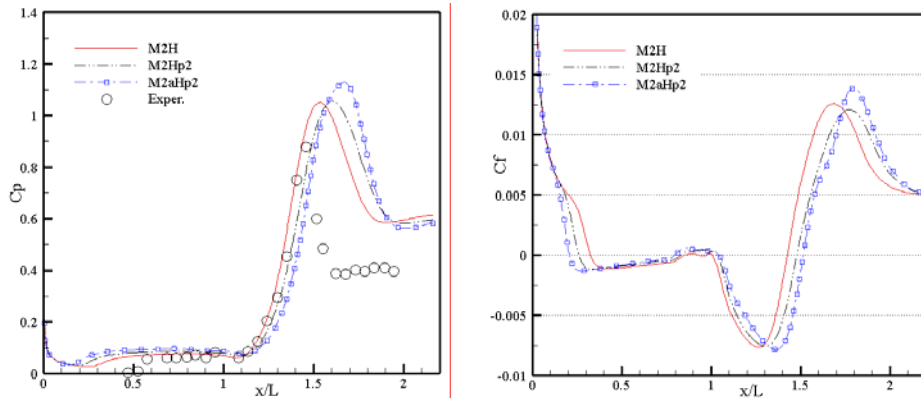


Figure 2. Pressure coefficient and skin friction coefficient on the mesh M2H using the one-step and two-step (p2) schemes

Contours of Mach number and specific mass for the meshes M2T, M2TR1 and M2TR2 with tetrahedral elements using the one-step scheme and the mesh adaption technique is shown in Fig. 3. The recirculation and recompression regions and the reflected shock wave are efficiently resolved with a mesh refinement using an automatic adaptive technique.

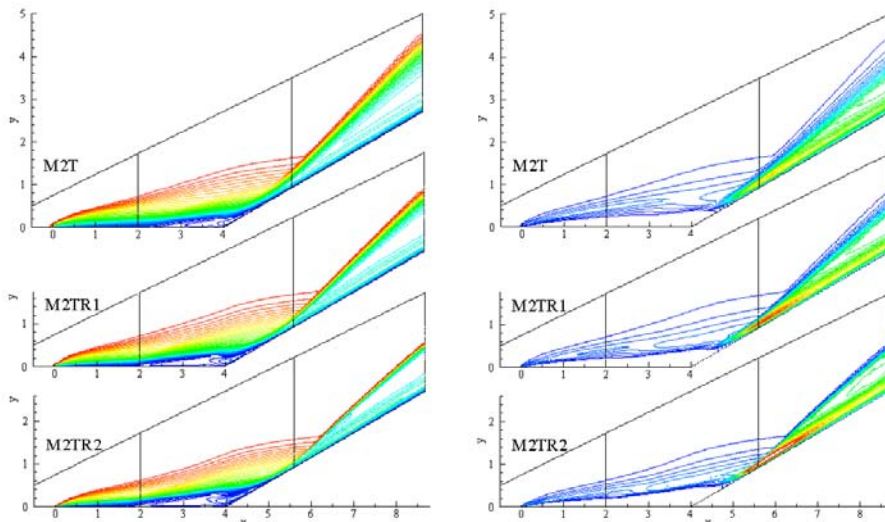


Figure 3. Mach number and specific mass contours on the meshes M2T, M2TR1 and M2TR2 with tetrahedral elements

The pressure coefficient and skin friction coefficient distributions, C_p and C_f , are shown in Fig. 4. This plot demonstrates the important role of the adaptive mesh refinement in capturing physical phenomena. M2TR2 mesh (two refinements levels) shows a good agreement with the experimental results presented by Holden *et al.* (2006), mainly in the recirculation region and the position and value of peak pressure. The computational results determined with the hexahedral meshes in the recompression region (Fig. 1) are slightly better than those obtained with tetrahedral meshes, but with the successive refinements the results in the M2T mesh are closer to those presented by Holden *et al.* (2006).

The value of the pressure coefficient in the plateau pressure region is approximately 0.61 with the M2T meshes; this value practically is coincident with the pressure coefficient obtained in the case of a non-viscous problem ($C_{p_{invisc}} = 0.628$). This difference is practically the same to that obtained with the hexahedral meshes.

The pressure coefficient and skin friction coefficient using tetrahedral meshes M2TR2 (one-step scheme) and M2Tp2R2 (two-step scheme) are plotted on Fig. 5, together with experimental and numerical results (Numer. 1 = Gnoffo, Numer. 2 = Tannehill) presented by Holden *et al.* (2006). Numerical results are in almost perfect agreement with the length of the interaction regions and the recompression region. The meshes M2T and M2Tp2 over predicted the pressures in the forebody region.

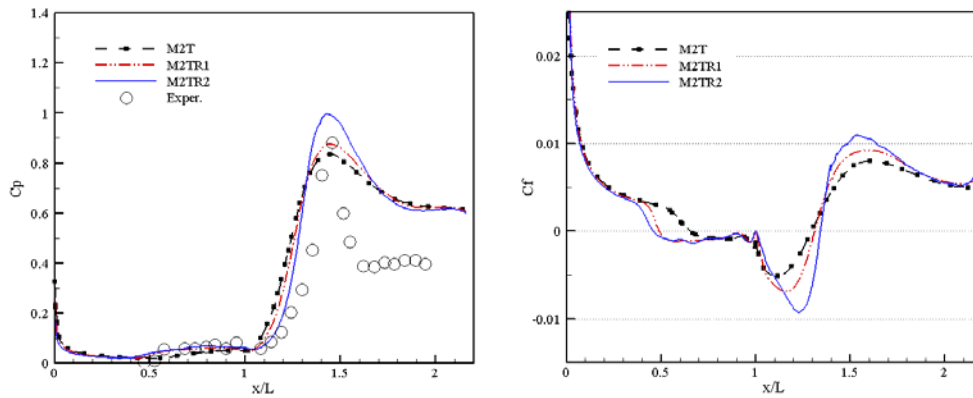


Figure 4. Pressure coefficient and skin friction coefficient on the meshes M2T, M2TR1 and M2TR2, compared with result obtained experimentally by Holden *et al.* (2006)

As shown in Fig. 5, while Gnoffo and Tannehill predictions of the pressure peak region achieve excellent agreement with experiments, the present computational results (M2TR2 and M2Tp2R2) overpredicts the pressure peak region. Nevertheless, the position of the peak pressure is better captured with the present simulation.

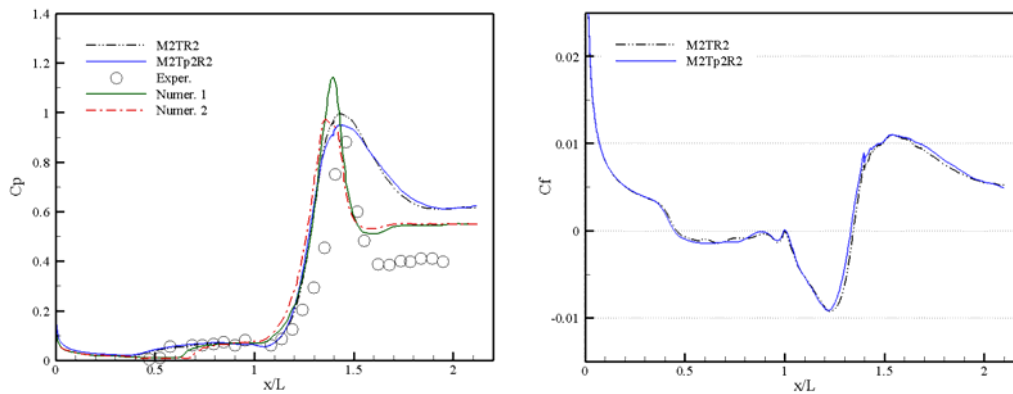


Figure 5. Pressure coefficient and skin friction coefficient on the meshes M2TR2 (one-step scheme) and M2Tp2R2 (two-step scheme), compared with result obtained experimentally by Holden *et al.* (2006)

Finally, with the purpose of analyzing the mechanism of shock wave / laminar boundary layer interaction, the pressure coefficient and skin friction coefficient in Fig. 6 shows the formation of a recirculation region and a shock wave at different non-dimensional times in the meshes M2T, M2TR1 and M2TR2. During the first stage ($t = 0.21$) is formed a small recirculation region (negative C_f) in the intersection region between the flat-plate and the ramp ($x/L = 1.0$). After this point the pressure has a slight peak due to the compression wave reattachment. After the recompression region the pressure value is approximately, $C_p = 0.60$, while for non-viscous problem C_p is about 0.628.

It should be noted that with time increase, the separation region length also increases. Initially the growth is greater on the flat-plate, and later on the ramp. The point of boundary layer reattachment remains practically fixed when time reaches $t = 3.15$, but the point of boundary layer separation moves continuously until $t = 4.428$. It must be observed that for the last two times showed in Fig. 6 ($t = 4.05$ and 4.428) the recirculation region grows less in comparison with the growth of the pressure peak.

The computed velocities profiles (v_1 and v_2) at stations $x/L = 0.25, 0.5, 0.75, 1.0, 1.25, 1.40, 1.50$ and 1.75 at the time $t = 4.428$ are displayed in Fig. 7. The abscissa is the component of velocity, and the ordinate is the distance measured normal to the wall. In Holden *et al.* (2006), the authors did not report experimental data for velocities, pressure and specific mass profiles.

The profile $x/L = 0.25$, is located upstream of the separation line and $x/L = 1.25$ is located downstream of the reattachment point. The skin friction coefficient increases rapidly downstream of the attachment due to the increase of the gradient on the stations $x/L = 1.40$ and 1.50 . The distortion of velocity profile is due to the shocks generated by the leading edge and the recirculation region.

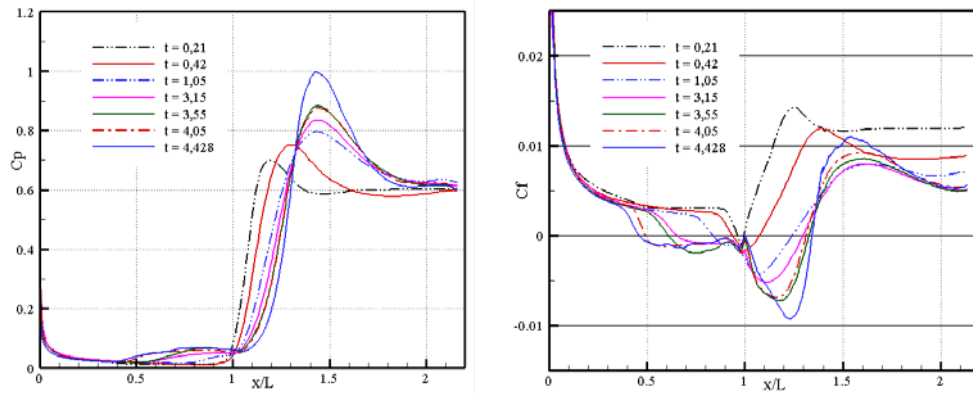


Figure 6. Pressure coefficient and skin friction coefficient on the meshes M2T/R1/R2 at different non-dimensional times

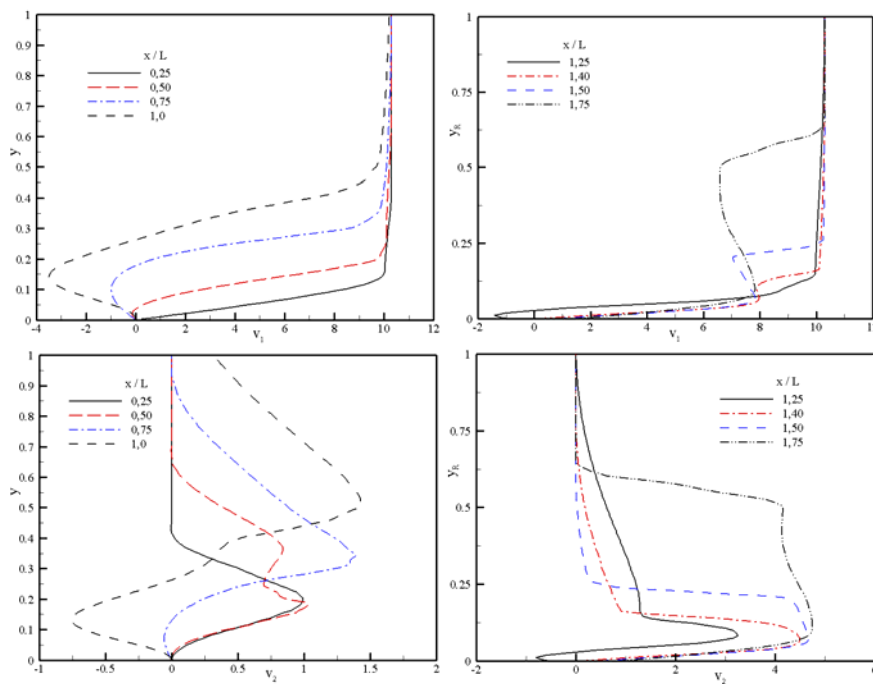


Figure 7. Velocities profiles (v_1 and v_2) at different stations (x/L)

Specific mass and pressure profiles are shown in Figs. 8 and 9. It can be observed that the specific mass and the pressure increase considerably after the reattachment point ($x/L = 1.40$ and 1.50).

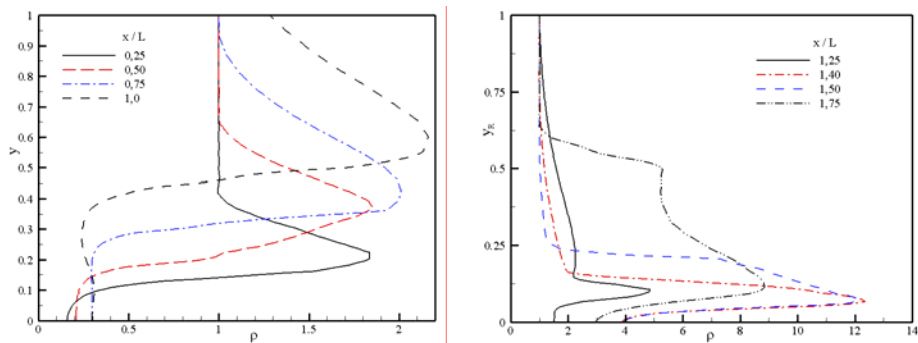


Figure 8. Specific mass profiles at different stations (x/L)

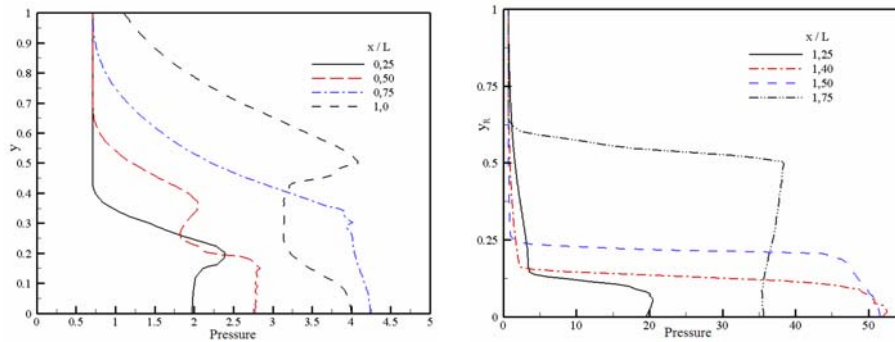


Figure 9. Pressure profiles at different stations (x/L)

2. CONCLUSIONS

In this paper we studied the shock wave/laminar boundary layer interaction over a compression corner with two explicit Taylor-Galerkin schemes in the context of meshes with hexahedral and tetrahedral elements. Based on the simulations examined in this study, no clear advantage was observed in choosing one scheme over the other, although it seems that the two-step algorithm is more diffusive with respect to the iterative one-step method; for this reason, results between these two techniques show some slight differences. The results presented in this paper have shown that the tetrahedral mesh with an adaptive technique presented solutions with better quality than the solution using hexahedral meshes. In the best Navier-Stokes solution the structure of the flow field was captured quite exactly with respect to the experimental model. The detailed characteristics of the distributions of pressure through the interaction regions were well predicted. A slight disagreement of the pressure on the forebody region was obtained. More tests need to be done to understand why the numerical solutions with hexahedral elements are inaccurate in some regions.

Based on the results obtained here, it may be concluded that an automatic adaptive technique have produced important improvements. Error indicators for low velocity components, change in the velocity direction, velocity gradients, pressure gradients and internal energy gradients, together with a mesh adaptation criterion identify correctly regions where refinements were necessary to obtain more accurate solutions. This test case also show that the use of a mesh adaptation procedure relieves the user from the tedious task of constructing an appropriate mesh and leads to a really optimal mesh that substantially reduces the amount of artificial dissipation needed in the flow solver.

3. ACKNOWLEDGEMENTS

The authors gratefully acknowledge the support of CAPES and CNPq.

4. REFERENCES

- Argyris, J., Doltsinis, I.S. and Friz, H., 1990 "Study on computational reentry aerodynamics", *Computer Methods in Applied Mechanics and Engineering*, Vol.81, pp. 257–289.
- Bono, G., 2008, "Simulação Numérica de Escoamentos em Diferentes Regimes utilizando o Método dos Elementos Finitos" (text in portuguese), Doctoral Thesis, PROMEC, UFRGS, Brazil.
- Chanetz, B., Benay, R., Bousquest, J.M., Bur, R., Pot, T., Grasso, F. and Moss, J., 1998, "Experimental and Numerical Study of the Laminar Separation in Hypersonic Flow", *Aerospace Science and Technology*, Vol.3, pp. 205-218
- Dolling, D.S., 2001, "Fifty Years of Shock-Wave/Boundary-Layer Interaction Research: What Next ?", *AIAA Journal*, Vol.39 (8), pp. 1517-1531.
- Donea, J., 1984, "A Taylor-Galerkin for convective transport problems", *International Journal for Numerical Methods in Engineering*, Vol.20, pp. 101–119.
- Holden, M.S., Waldhams, T.P., Harvey, J.K and Candler, G.V., 2006, "Comparison between Measurements in Regions of Laminar Shock Wave Boundary Layer Interaction in Hypersonic Flows with Navier-Stokes and DSMC Solutions", OTAN RTO-TR-AVT-007-V3.
- Kawahara, M. and Hirano, H., 1983, "A finite element method for high Reynolds number viscous fluid flow using two step explicit scheme", *International Journal for Numerical Methods in Fluids*, Vol.3, pp. 137–163.
- Popiolek, T.L. and Awruch, A.M., 2006, "Numerical Simulation of Incompressible Flows using Adaptive Unstructured Meshes and the Pseudo-compressibility Hypothesis", *Advances in Eng. Soft.*, Vol.37, pp. 260-274.

5. RESPONSIBILITY NOTICE

The authors are the only responsible for the printed material included in this paper.